1 **Effect of wand-type underdrains on the hydraulic performance of pressurised sand**

2 **media filters**

3

4 Toni Pujol[a], Jaume Puig-Bargués[b], Gerard Arbat[b], Miquel Duran-Ros[b], Carles Solé-Torres[b],

5 Joan Pujol[b], Francisco Ramírez de Cartagena[b]

6

7 [a]Department of Mechanical Engineering and Industrial Construction, University of Girona, c/

8 Universitat de Girona 4, 17003 Girona, Catalonia, Spain.

9 [b]Department of Chemical and Agricultural Engineering and Technology, University of Girona,

10 c/ Maria Aurèlia Capmany 61, 17003 Girona, Catalonia, Spain.

11

12 **Abstract**

13 Sand media filtration is frequently used in drip irrigation systems. Commercial filter designs

14 may use different underdrain models but wand-type designs provides a large ratio of horizontal

15 area covered by underdrains and are expected to provide a uniform flow of water through the

16 medium. The complexity of these designs makes it difficult to analyse the effects of changing

17 the position of wand and the slot open area. These underdrain effects were studied by means

18 of a computational fluid dynamics (CFD) model assuming clean water conditions. The

19 backwashing process was not considered. The results obtained from the numerical model were

20 validated using experimental data from a commercial sand media filter with 10 wands.

21 Unbalanced flows between underdrains were observed in the original configuration. Two new

22 designs were proposed: (1) a design that uses the same type of wands as the original filter but

23 distributes them so as to have an equal horizontal area served by each wand; (2) a design that

24 uses the same spatial distribution as the original filter but with longer wands in those regions

25 of the original filter with lower volumetric flow. CFD simulations of the two designs indicate

26 that design (1) can reduce the pressure drop through the filter at nominal volumetric flow rates

27 by up to 5.8% with a more uniform flow inside the medium and design (2) could improve the

28 performance of the filter by achieving an up to a 4.9% reduction of pressure drop. Thus, the

29 spatial distribution of underdrains is a key parameter in the hydraulic performance of sand

30 media filters.

31

32 **Keywords:** Filtration; Granular bed; Drip irrigation; Computational fluid dynamics; Modelling

33

34

35

1. Introduction

The worldwide area of agricultural land irrigated with microirrigation systems increased by 45% from 2013 to 2018, with increases of 20% and 60% in developed and developing countries, respectively (ICID, 2019). The adoption of more efficient irrigation techniques such as microirrigation can improve water and land productivity, but it increases energy and investment requirements (Tarjuelo et al., 2015). Moreover, emitter clogging is a major problem in microirrigation systems (Nakayama, Boman Pitts, 2007) since shortens the system longevity, which can seriously affect the economic competitiveness of these systems (Lamm & Rogers, 2017). Emitter clogging is directly related to the quality of irrigation water, and it is usually worsened when effluents (Gamri, Soric, Tomas, Molle, Roche, 2014; Green, Katz, Tarchitzky, Chen, 2018) or brackish waters (Lili et al., 2016) are used.

Filtering irrigation water properly and effectively prevents emitter clogging. Sand media filters are the most commonly used filtration protection for microirrigation systems when low quality waters are used (Trooien & Hills, 2007). Their simplicity and large filtration volumes make them favoured by farmers and designers over other filter types (Burt, 2010). In comparison with other parts of the irrigation system, sand media filters can have higher pressure requirements mainly due to backwashing (Burt, 2010). However, substantial differences in pressure loss and media cleaning are found between filters of different designs (Burt, 2010). Thus, the study of the hydraulic performance of the different sand media filters is necessary to improve their designs since they have an effect on particle removal, energy consumption and emitter clogging (Solé-Torres et al., 2019a, 2019b).

The head loss of different sand media filters filled with different grain sizes and operating at different velocities is significantly affected by the filter internal elements, mainly the diffuser plate and the underdrain (Mesquita, Testezlaf & Ramirez, 2012). Computational fluid dynamics (CFD) is a tool that allows the hydrodynamic simulation of irrigation equipment for assessing its performance and the effect of design improvements. This technique was used by Mesquita, de Deus, Testezlaf, da Rosa and Diotto (2019) for designing a new diffuser plate that reduced the vortex formation close to the sand bed surface, thereby achieving less bed deformation and avoiding preferential flow paths that can cause filters to be less effective since they are not backflushed sufficiently well when preferential paths are formed (Enciso-Medina, Multer & Lamm, 2011). Arbat et al. (2011, 2013) used CFD and analytical equations to assess head losses across a sand media filter with a nozzle underdrain and verified that non uniform flow was produced in the underdrain area. Different improvements of the nozzle design were

69 evaluated with CFD by Bové et al., (2015) and using analytical equations by Pujol et al., (2016)
70 The work produced a new improved underdrain prototype that reduced pressure loss across the
71 underdrain by 20 - 45% compared to commercial designs (Bové et al., 2017). The
72 improvements carried out by Bové et al. (2017) were assessed by both CFD simulation and
73 experiment and consisted of enlargement of the passage at the underdrain outlet; reduced flow
74 curvature when approaching to the underdrain by changing the underdrain slots; replacing the
75 media size where there is more flow curvature with media of greater size to increase hydraulic
76 conductivity in these areas.
77 Other common types of underdrain design that can be found in sand media filters used for
78 microirrigation systems use wands (Burt, 2010). The higher pressure losses and the removal of
79 particles near to the the walls have been observed with this type of underdrain design (Mesquita
80 et al., 2012) but these effects have not been fully investigated since a complete hydraulic study
81 of the performance of wand filters has not been carried out.
82 Thus, the main objective of this paper was to analyse the hydraulic performance of wand-type
83 sand media filter underdrains during the filtration process using clean water conditions in order
84 to suggest design improvements that could improve flow circulation and reduce pressure loss.
85 The backwashing process was not considered in this study.
86
87 **2. Materials and methods**
88 2.1 Experimental layout
89 A commercial sand media filter with wand underdrains (FA1M, Lama, Gelves, Spain) was
90 installed in a drip irrigation system (see Fig. 1).The filter was filled either with 62.5 kg or 94
91 kg of silica sand, providing an effective height over the centre of the wands equal to 200 mm
92 or 300 mm, respectively. Silica sand CA-07MS (Sibelco Minerales SA, Bilbao, Spain) with an
93 effective diameter (D_e, sieve size opening that will pass 10% of sand) of 0.48 mm and a
94 coefficient of uniformity (ratio of the size opening which will pass 60% of the sand through
95 the size opening which will pass 10% through) of 1.73 was used. No evaluation of possible
96 sand losses during the filtration process was carried out. The filter had 500 mm inner diameter
97 with 10 wand-type underdrains horizontally positioned at 60 mm intervals (see Fig. 2). Each
98 one of the 10 wands consisted of 24 slots 79 mm long and 0.5 mm wide, radially distributed in
99 four groups of six at 11 mm from the centre line (see Fig. 3). The total slot open area was 9600
100 mm^2. By comparison, the pipes at both filter inlet and outlet had inner cross-sectional areas
101 equal to 1300 mm^2. It should be noted that two small reinforcement rings were used in the

102 actual wands but were not simulated in the CAD representation in order to provide a feasible

103 mesh size.

104 The volumetric flow rate was measured using an Isomag MS2500 flowmeter (ISOIL Industria

105 SpA, Cinisello Balsamo, Italy), with a measurement range from 0 to 63 m^3 h^{-1} and a reading

106 accuracy of $\pm 1\%$. Pressure values were obtained at 1.44 m head before the filter inlet and 1.29

107 m after the filter outlet (see Fig. 1) using a MBS4010 pressure transmitter (Danfoss, Nordborg,

108 Denmark) with flux diaphragm with a measurement range from 0 to 600 kPa and a full scale

109 accuracy of $\pm 0.3\%$. Data were collected at 1 min interval. Inlet water came from the tertiary

110 effluent of a wastewater treatment plant (see, Solé-Torres et al. (2019a) for details). It was

111 assumed that the hydraulic performance of the filter in clean conditions corresponded to that

112 occurring during the first five minutes after backwashing. The filter was assumed as being far

113 from being clogged during this period and the results were interpreted as equivalent to those

114 obtained when using clean water. Table 1 shows the operational conditions for the four

115 experimental cases analysed, each one obtained from averaging the first five minutes of a

116 minimum of 33 cycles during 20 d. The average time interval between two consecutive

117 backwashing cycles for cases 1, 2, 3 and 4 of Table 1 were 227, 364, 261 and 169 min,

118 respectively.

119

120 Table 1. Experimental pressure drop Δp_e as a function of the volumetric flow rate Q and height of the

121 sand surface above the underdrain centre H for the experimental cases analysed.

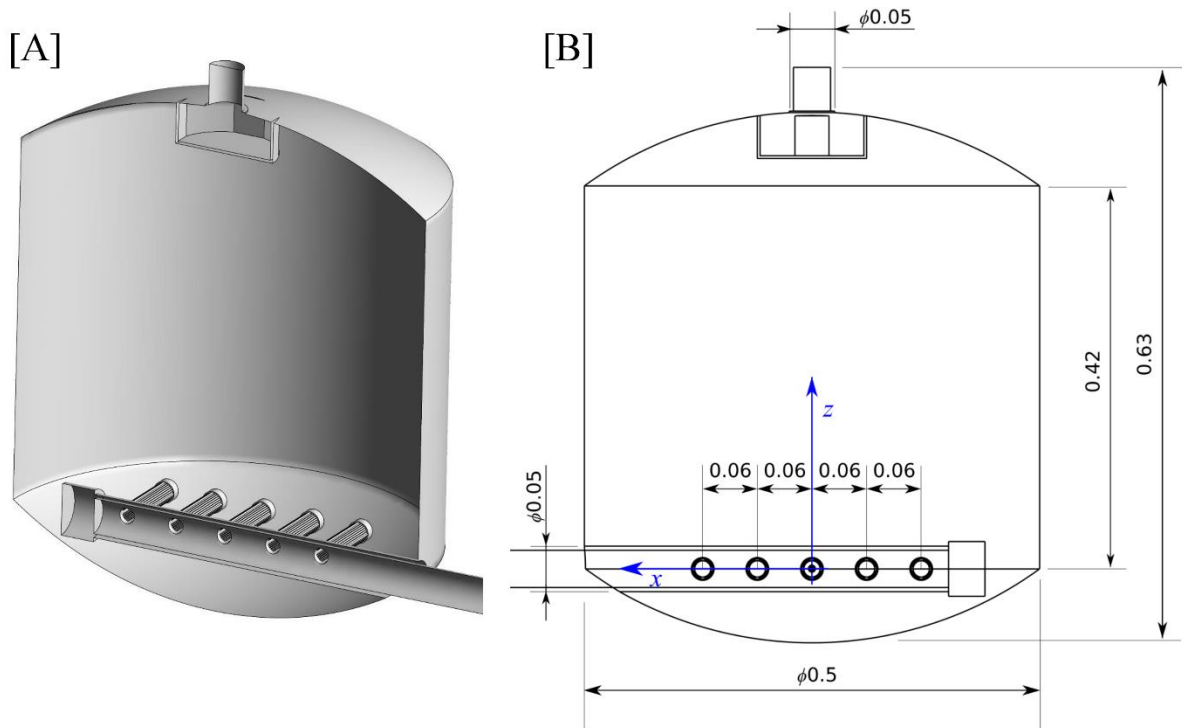| Experimental case	H (mm)	Q (m^3 h^{-1})	Δp_e (kPa)
1	200	6.0 ± 0.2	18.7 ± 1.1
2	300	6.0 ± 0.1	21.1 ± 1.1
3	200	12.0 ± 0.2	43.8 ± 1.1
4	300	11.8 ± 1.9	49.0 ± 1.1

122

123

124

4

125
126   Fig. 1 - View of the experimental setup. A and B indicate the location of the pressure
127   transmitters before and after the filter, respectively, in filtration mode.
128

129
130

131   Fig. 2 – [A] Cross-sectional view of the sand media filter analysed (Lama FA1M type) that
132   uses 10 wands. [B] Main dimensions of the filter (in m). The blue coordinate axes located at the
133   symmetry plane are used in the analysis.
134

[A]   [B]

135

136
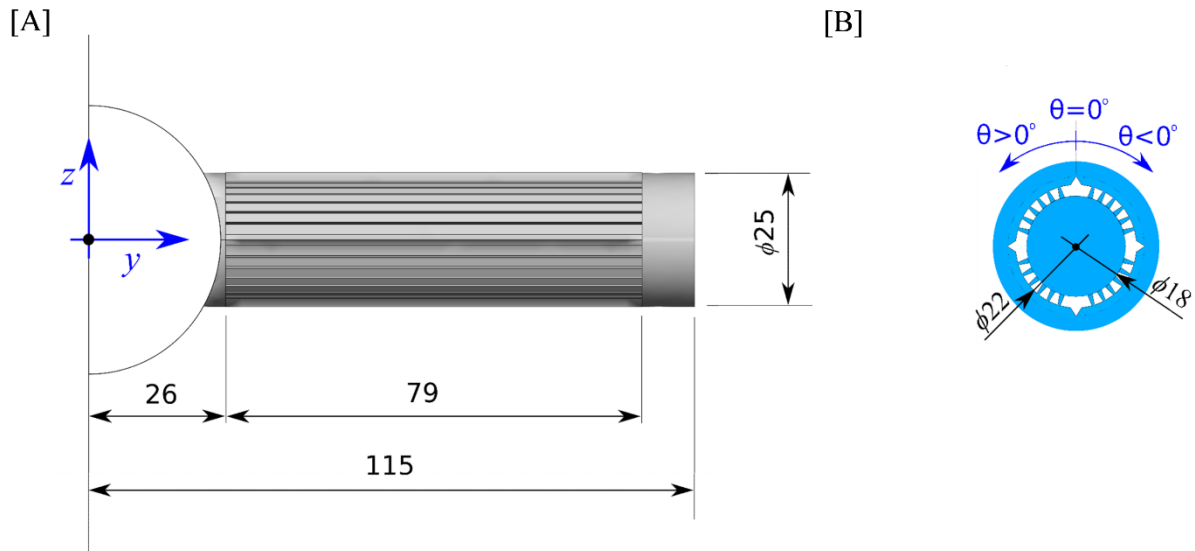
Fig. 3- [A] Main dimensions of a wand (in mm). [B] Cross-sectional (*x-z* cut) detail of the wand (view

towards the *y* = 0 plane). The flow passage zones are highlighted in blue. Each wand has 24 slots 79

mm long and 0.5 mm wide.

2.2 Model set-up

The numerical model here employed was ANSYS-Fluent (version 19.1), a commercial CFD code that has successfully been applied in previous studies of sand media filters (Arbat et al., 2011; Bové et al., 2017). ANSYS-Fluent uses a finite volume method to solve the fluid flow governing equations in a discretised domain formed by small elements (i.e., the mesh) (ANSYS, 2018). Here, the domain analysed was reduced to a half section of the filter (Fig. 2) by taking advantage of symmetry. This substantially reduced the computational time without compromising the accuracy of the results. The sand medium was simulated as a porous region with fixed height. Therefore, the filter domain was divided into three main regions: 1) the water-only upper region that includes the inlet; 2) the porous lower region that contains the medium; 3) the water-only region at the filter exit (inner wands and exit pipe).
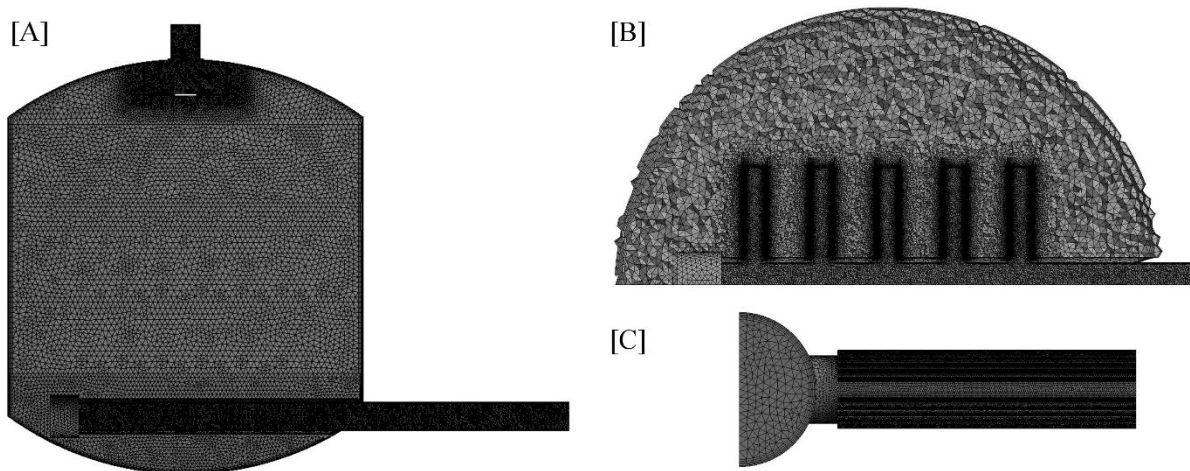
Fig. 4 – [A] Mesh at the symmetry plane. [B] Detail of mesh at the *x-y* plane at *z* = 0. [C] Detail of mesh in one wand.

These regions had unstructured meshes created with ANSYS-Meshing software. The mesh was highly refined near the wands and, also, at both inlet and exit regions (Fig. 4). Triangles were used to mesh all surfaces. A layer of five prisms was attached to solid walls that grows towards the fluid volume. Tetrahedrons were employed in the inner volume of all regions. The maximum characteristic size of surface elements (triangles) at the slots of the wands was 0.2 mm and the maximum characteristic size of volume elements (tetrahedrons) ranged from 2 mm at the exit pipe to 7 mm at the inner zone of the sand media (far from wands and diffuser plate). The number of elements employed per region were: $1.3{\times}10^6$ elements for the water-only region at the top of the filter ($H = 300$ mm case), $11.6{\times}10^6$ elements in the sand media ($H = 300$ mm case), $5.0{\times}10^6$ elements for the water-only region at the exit of the filter. Thus, $18.0{\times}10^6$ elements were used to mesh the whole filter domain. A detailed mesh sensitivity study was carried out, being explained in subsection 2.4.

Boundary conditions included a fixed pressure at the filter inlet and a fixed mass flow rate at filter outlet, both values were specified to be in agreement with the experimental data. A symmetry boundary condition was applied to the plane of symmetry (*x-z* plane at *y* = 0). Finally, all solid walls were defined as non-slip surfaces with a surface roughness value equal to 0.1 mm in order to simulate slightly corroded steel surfaces.

The numerical algorithm used double precision. The fluid flow governing equations were the classical Navier-Stokes ones for incompressible flows under stationary conditions, with the SIMPLE calculation scheme for the pressure-velocity coupling and second order schemes for the spatial discretization of all variables. The flow in the porous media (region identified as

178 sand) was modelled by adding a sink in the standard momentum equations. This term led to a

179 pressure gradient ∇p in the porous media (Pa m^{-1}) that followed

$$-\nabla p = \frac{1}{\alpha}\mu v_i + C_2 \frac{\rho}{2}|v|v_i \quad for\ i = x, y, z \tag{1}$$

180 where v_i is the i-th component of the flow velocity (m s^{-1}), $|v|$ is the magnitude of the flow

181 velocity (m s^{-1}), μ is the fluid viscosity (Pa s), ρ is the fluid density (kg m^{-3}), α is the

182 permeability of the filtration medium (m^2) and C_2 is the inertial resistance factor (m^{-1}).

183 The turbulence model used was the standard k-ω that performs similarly to the realisable k-ε

184 model but it was expected to have a superior performance in low Reynolds number flows

185 occurring inside the sand filter. For comparison, differences less than 0.5% were obtained for

186 pressure drop values across the filters when using the realisable k-ε turbulence model instead

187 of the standard k-ω one for the $H = 300$ mm, $Q = 6$ m^3 h^{-1} case. At both the inlet and outlet

188 boundaries, the turbulent viscosity ratio was set to 10% and the turbulence intensity was set to

189 5%.

190 In all simulations the convergence criterion was set to 10^{-5} for the maximum value of the

191 residuals of the variables, including those of the turbulence model. Once this value was

192 achieved, the model ran for a minimum of 500 more iterations. Thus, the variation of the

193 computed values as a function of the iteration was very small. For example, a variation of total

194 pressure drop < 0.5 Pa was found between iteration m-100 and iteration m, m being the last

195 iteration chosen to report the data.

196

197 2.3 Model calibration

198 Both viscous (1/α) and inertial (C_2) factors in Eq. (1) were fitted to minimise the difference

199 between experimental data and simulations. The root mean square relative error $RMSrE$ was

200 the function to chosen to be minimised, where,

$$RMSrE = \sqrt{\frac{\sum_{i=1}^{n}\left(\frac{\Delta p_{m,i} - \Delta p_{e,i}}{\Delta p_{e,i}}\right)^2}{n}} \tag{2}$$

201 with $\Delta p_{e,i}$ the experimental pressure drop obtained in the i-th case (Pa), $\Delta p_{m,i}$ the pressure drop

202 predicted by the model applying the conditions of the i-th case (Pa) and n ($= 4$) the number of

203 cases experimentally analysed (see Table 1).

204 The numerical model was run for all the four conditions in Table 1 by varying the values of the

205 viscous α^{-1} and inertial C_2 factors at intervals of $\Delta(\alpha^{-1}) = 10^4$ m^{-2} and $\Delta C_2 = 0.2 \times 10^9$ m^{-1}. The

206 pressure drop of the external conduits was added to that simulated for the filter in order to
207 obtain the $\Delta p_{m,i}$ value used in Eq. (2). These external head losses were required in order to
208 properly compare with the experimental measurements $\Delta p_{e,i}$ with simulations since field
209 manometers were located at a given distance from inlet and outlet of the filter (see section 2.1).
210
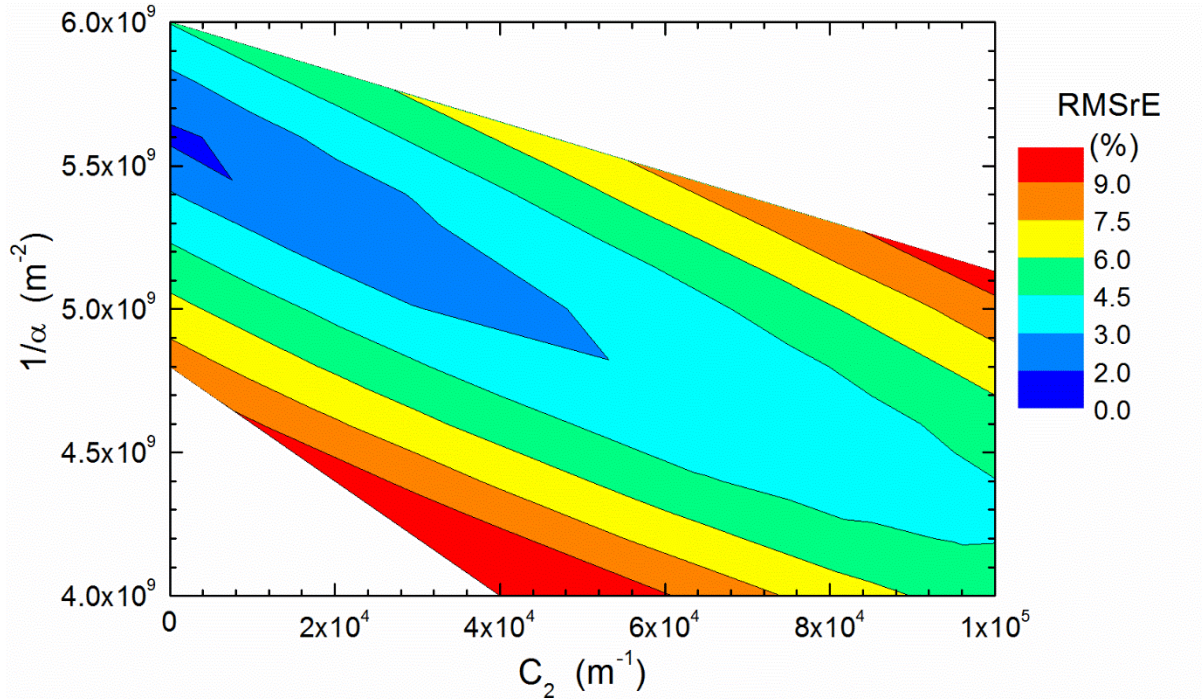
212 Fig. 5 - Contours of root mean square relative error (see Eq. (2)) as a function of the viscous factor
213 $1/\alpha$ and the inertial factor C_2.

214

215 The grid of points obtained from Eq. (2) were used to represent contours of the *RMSrE* value
216 (Fig. 5). Blank regions in Fig. 5 indicate zones not simulated. Viscous and inertial coefficients
217 with similar *RMSrE* values do not necessarily predict equal values of individual (i.e., per *i*-th
218 case) pressure drops. The minimum *RMSrE* value, expressed in %, was attained with $\alpha^{-1} = 0$
219 m^{-2} and $C_2 = 5.6 \times 10^9$ m^{-1} (*RMSrE$_{min}$* < 1.9 %).

220
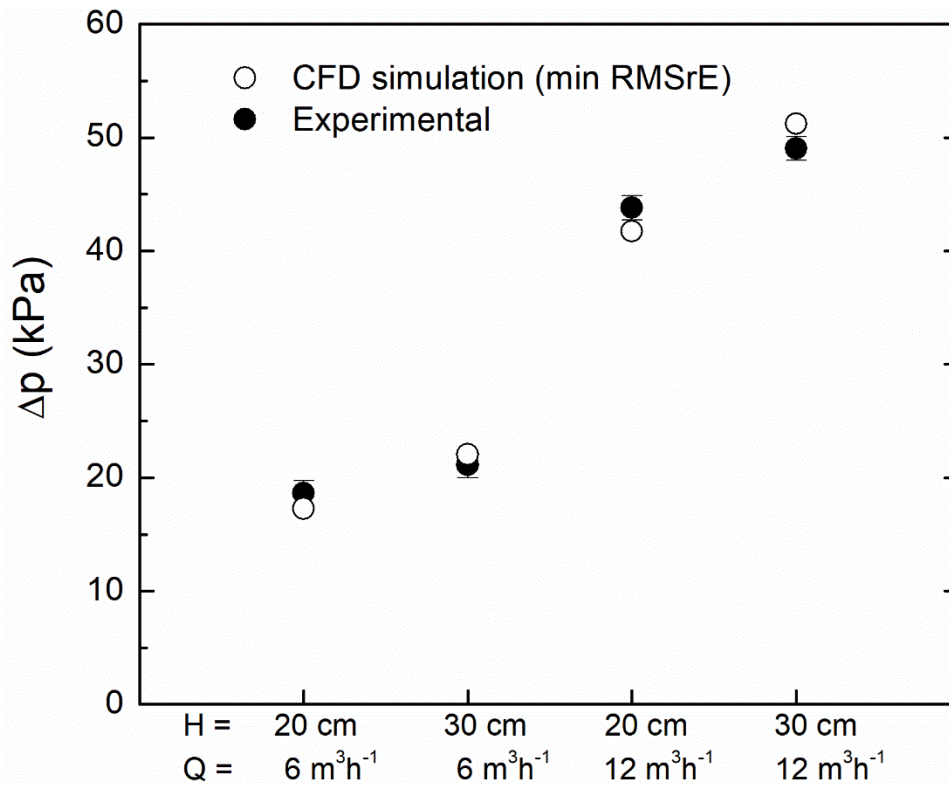
221

222 Fig. 6 - Experimental (solid circles) and simulated (open circles) pressure drops with viscous and

223 inertial factors that minimise the root mean square relative error ($1/\alpha = 0$ m^{-2}, $C_2 = 5.6 \times 10^9$ m^{-1}).

224

225 With these values of viscous and inertial factors, the pressure drop of the system predicted by

226 the model in comparison with the experimental data (Table 1) is shown in Fig. 6 for the 4 cases

227 analysed. Although the *RMSrE* value was < 1.9%, the maximum difference of pressure drop

228 between measurement and simulation occurred for the $H = 200$ mm and $Q = 12$ m^3 h^{-1} case

229 being equal to 2.3%. Note that simulations tended to underestimate the pressure drop when H

230 = 200 mm and to overestimate it when $H = 300$ mm. However, the conclusions of the present

231 work are not affected by the exact values employed in Eq. (1).

232

233 2.4 Mesh sensitivity

234 A mesh sensitivity study was carried out with the values of both viscous and inertial factors

235 determined above. The filter pressure drop when using different meshes was analysed. The

236 coarse mesh was defined by increasing the main characteristic lengths of the finer mesh defined

237 in section 2.2 by a factor of 3. The regular mesh applied an increment by a factor of 1.5 with

238 respect to the finer mesh. Thus, the total number of elements of the course, regular and fine

239 meshes were 2.7×10^6, and 8.9×10^6 and 18.0×10^6 elements, respectively. The difference of the

240 pressure drop value between the fine and the regular mesh was < 0.35% and between the fine

10

241 and the coarse mesh was $< 0.57\%$. With these values, the grid independence index (GCI^{21}_{fine})

242 was therefore $< 0.1\%$ with an order $p = 7.2$ (Célik et al., 2008). Therefore, the results presented

243 below were grid independent.

244

245 **3. Results and discussion**

246 3.1. Original filter

247 Unless otherwise stated, results discussed in this section correspond to the $H = 300$ mm and Q

248 $= 6$ m^3 h^{-1} case. Nevertheless, the main findings pointed out below were also observed when

249 analysing the other cases listed in Table 1.

250 Here the pressure values inside the filter are first studied. Figure 7 shows the pressure profile

251 in three vertical lines ($y = 70$, 140 and 210 mm) located at the y-z plane at $x = 0$ m (see Figs. 2

252 and 3 for plane definitions). Pressure contours at the $z < 180$ mm are shown for clarity. Pressure

253 values were almost equal for the three lines above $z > 200$ mm. This height corresponds to 100

254 mm below the sand surface (located at 300 mm). In this 100 mm layer, the flow behaved as if

255 no underdrain existed, being very uniform throughout the entire cross-sectional area of the

256 filter. Since the velocity of the flow in this region had almost a unique z-component, the

257 pressure decreased linearly with depth (following Eq. (1)). Below $z = 200$ mm, the influence

258 of the underdrain on the pressure drop increased with depth, being more intense when

259 approaching the wand. Thus, following a vertical line above the underdrain ($y = 70$ mm in Fig.

260 7), pressure decreased more rapidly than linear. This was a consequence of the increase in flow

261 velocity within the sand media in the vicinity of the wand slots. By contrast, pressure slightly

262 reduced with depth in a vertical profile far from the underdrain (e.g., $y = 210$ mm in Fig. 7)

263 since the flow velocity in that region was very low.

264

265

266
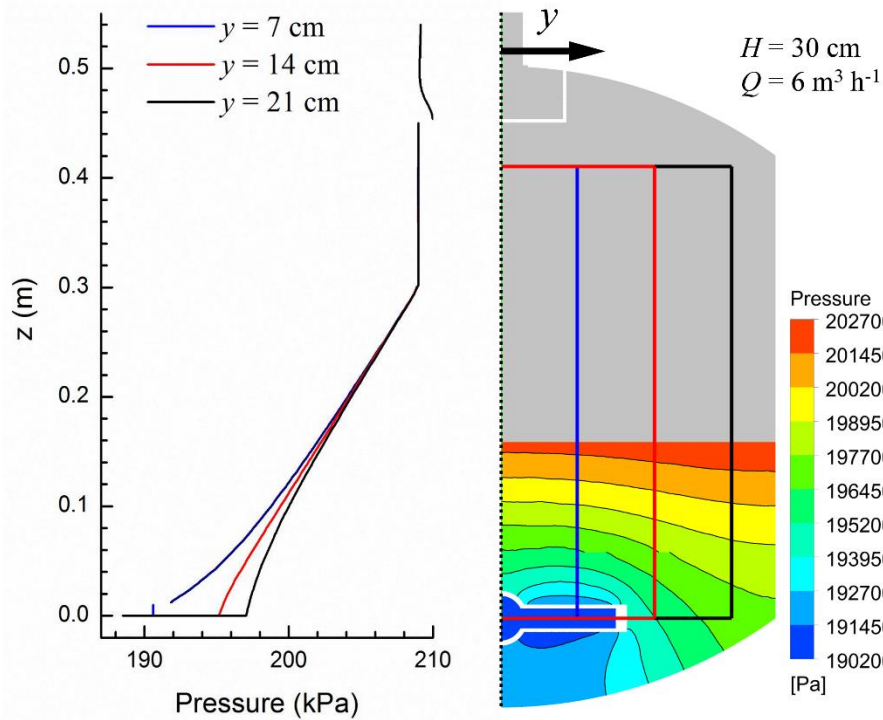
Fig. 7 - Pressure profiles (left) through the lines shown at right (plane located at $x = 0$ m). Pressure contours are only displayed at the bottom region for a better visualization. Case $H = 300$ mm, $Q = 6$ $m^3\,h^{-1}$.

The diffuser plate may have a strong effect on the filter. It substantially increased the pressure of the incoming flow (see Fig. 7) and diverted the flow in different directions. Figure 8 shows the contours of vertical velocity in the horizontal plane at four different heights, varying from $z = 450$ mm (diffuser plate) to $z = 310$ mm (just 10 mm above the sand surface). Flow primarily descended in the external region close to the walls, and in the central zone close to the sand top surface (Fig. 8). Other regions showed upward flows indicating the existence of vortices in the water-only region. An ideal filter design should produce uniform downward flow values close to the top of the medium to avoid causing an uneven sand surface. A bumpy sand surface at the top of the medium may indicate the existence of preferential flow patterns, thereby reducing the hydraulic performance of the filter.
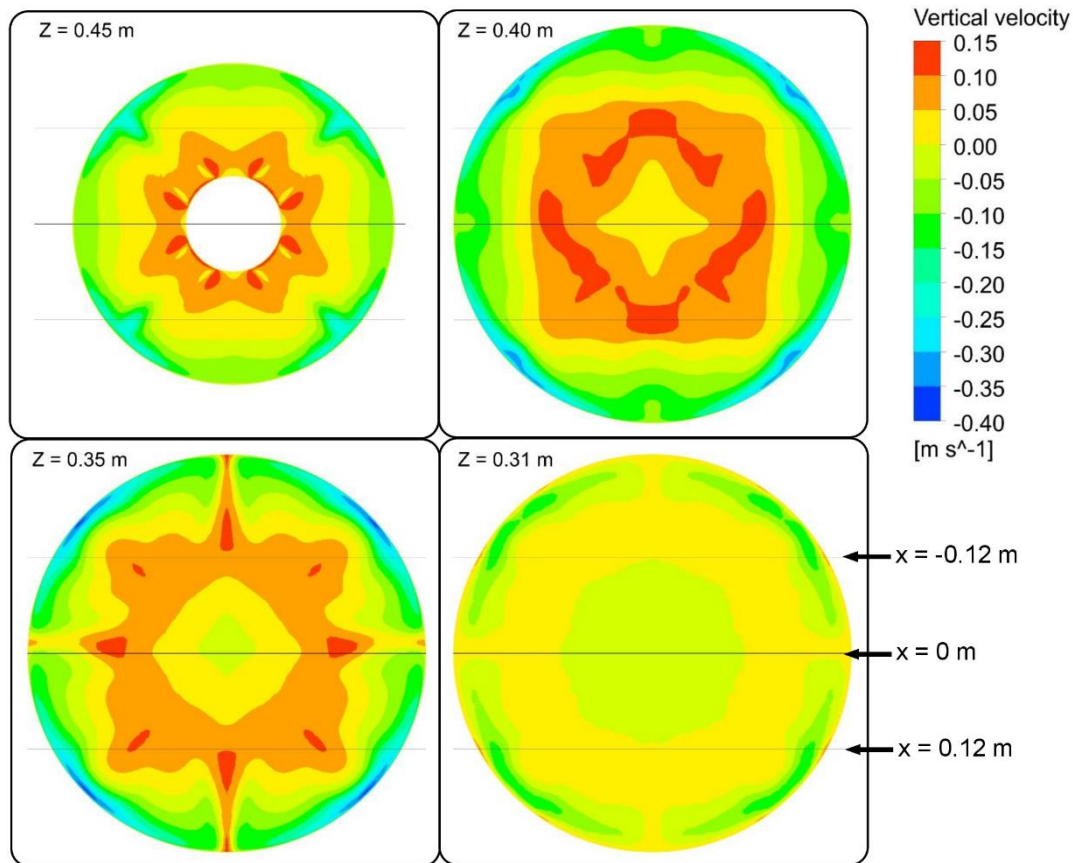
Fig. 8 - Contours of vertical velocity at four different horizontal *x-y* planes. The horizontal lines at different *x* values indicate the location of the *y-z* planes shown in Fig. 9. Case $H = 300$ mm, $Q = 6$ m³ h⁻¹.

The regions of vorticity at the top of the filter can be clearly seen in Fig. 9, where the velocity vectors in the vertical *y-z* plane are shown at different positions, with $x = 0$ being the central one. According to Fig. 2b, the position $x = 0.12$ m corresponds to the centre of the first row of wands (the ones closer to the exit). The height of the centre of the vortex reduced away from the central plane ($x = 0$). This implied higher velocity values near the top of the medium, favouring the existence of rough surfaces there. The relevance of the diffuser plate in the performance of sand media filters has extensively been studied by Mesquita et al. (2019).

At the underdrain level, Fig. 9 also reveals differences in flow patterns. Velocities were maximum at the centre of the first wand ($x = 0.12$ m), almost doubling the values obtained at the centre wand ($x = 0$ m). This phenomenon can be clearly seen in Fig. 10, where the contour velocities in the horizontal *x-y* plane ($z = 0$) are shown. Considering an individual wand, flow velocity increased approaching the connection with the central collector. This effect was more significant with wands located at both extreme positions (1 and 5). The maximum velocity of

302   the water flow (= 1.76 m s^{-1}) found in the filter occurred in the exit collector at the end of wand

303   1. Figure 10 indicates that this high velocity region is accompanied by a low velocity region

304   with recirculating flow. This hydraulic behaviour (high velocity with an attached recirculation

305   zone) was commonly observed in bending flows exiting surfaces with sharp edges. Although

306   this effect was also observed with all wands, it was intensified at the exit of wand 1 since all

307   the flow from downstream wands was added to the main collector. This increase in volumetric

308   flow rate along the exit collector reduced the pressure along it, reaching a minimum value just

309   after wand 1 (e.g., reduction of 1.8 kPa in the area averaged pressure of the exit pipe cross

310   section from the position of wand 5 to that of wand 1). Once the flow exited the filter, pressure

311   continuously dropped in the pipe following the standard friction losses term. Note from Fig.

312   10 that the flow attains fully developed conditions at the end of the filter exit pipe.

313
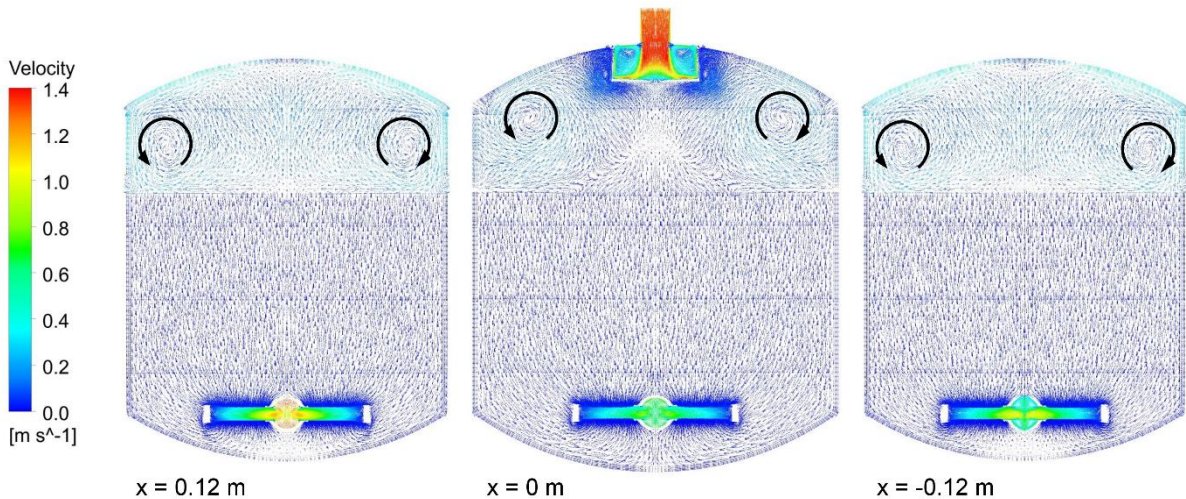
314

315   Fig. 9 - Velocity vectors at three different *y-z* planes (see Fig. 8). Arrows indicate the direction of

316   vortices. Case $H = 300$ mm, $Q = 6$ m^3 h^{-1}.

317

318   Within the sand, the flow velocity was highly non-uniform when approaching the slots of the

319   wands. This irregular distribution of the water flow reduces the effectiveness of the drainage

320   process as pointed out by Mesquita, Testezlaf, de Deus, and da Rosa (2017). Figure 11 shows

321   the velocity contours in a cylindrical shell of radius 12 mm collinear with the wand axis 1 and

322   3. The blank regions in Fig. 11 at $\theta = 0$º, ±90º and ±180º correspond to the wand reinforcement

323   bars (see Fig. 2b). The six longitudinal slots per 90º angle are located at a radius of 11 mm,

324   being only 1 mm below the shell depicted in Fig. 11. These slots are located just below the

325   regions where peak water velocities occur. Figure 11 shows that upper slots (-90º < θ < 90º)

326   were the main zones for circulating water. By contrast, slots at the below the wands weakly

14

327 contributed to the total flow rate. A common feature to all slots is the fact that at both ends the
328 velocities reached their maximum values. This is most likely because at these points there was
329 a larger concentration of volumetric flow from regions not occupied by wands. This was more
330 pronounced at the outer edge of the slot since the area not occupied by the underdrain was
331 substantially larger, especially at wand 3 (see, e.g., Fig. 7b or Fig. 10). Comparing wands #1
332 and 3 showed an unbalanced functioning between them, with a higher contribution to the water
333 flow for the first underdrain since it had to serve a larger sand region. Note that, in comparison
334 with the water-only region (e.g., Fig. 10), flow velocities within the sand region were, at least,
335 one order of magnitude lower.
336
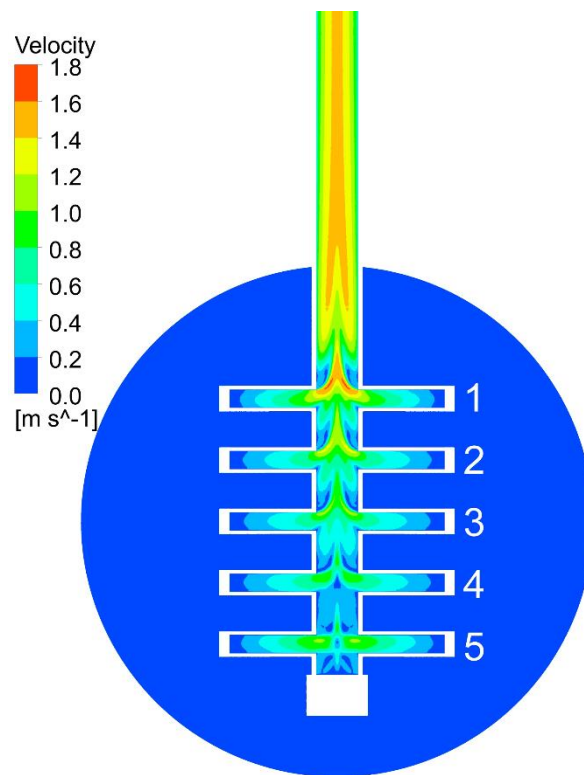
337
338 Fig. 10 - Velocity contours at $z = 0$. Wands are centred at $x = 0.12$ m (1), $x = 0.06$ m (2), $x = 0$ m (3), x
339 $= 0.06$ m (4) and $x = -0.12$ m (5). Case $H = 300$ mm, $Q = 6$ m^3 h^{-1}.
340
341
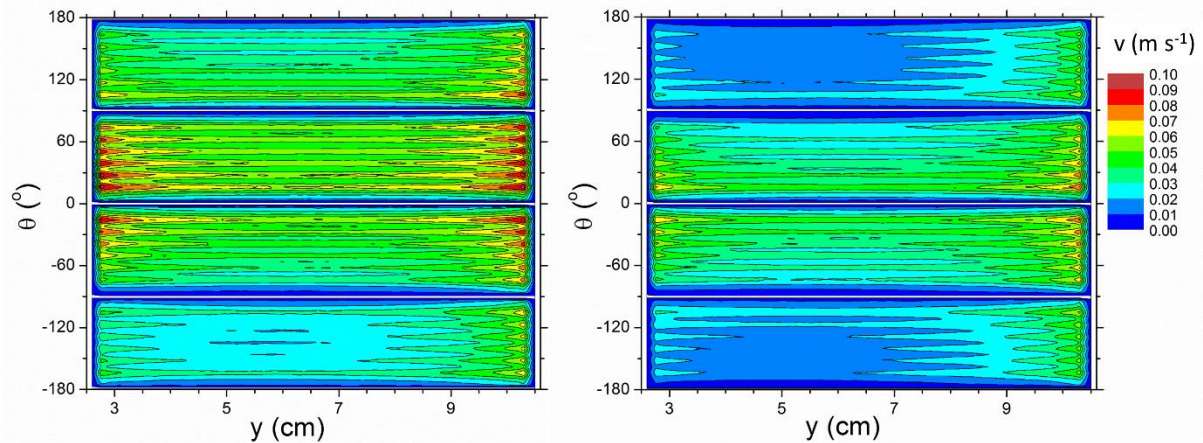
Fig. 11 - Velocity contours through a cylindrical shell of 12 mm radius around wand 1 (left; $x = 0.12$ m) and wand 3 (right; $x = 0$ m). See Fig. 2b for the definition of the θ angle. Case $H = 30$ cm, $Q = 6$ m^3 h^{-1}.

The contribution to the volumetric flow rate for each one of the 24 slots per wand at positions 1, 3 and 5 is depicted in Fig. 12. Positive angles face towards the exit of the filter. The central wand (3) behaved symmetrically, with a maximum flow rate found in the upper slots ($= 0.0093$ l s^{-1}). The minimum contribution to the flow rate was at angle $\theta = \pm140.7°$ ($= 0.0039$ l s^{-1}). The minimum flow rate was not found at the lowermost slot ($\theta = \pm163.6°$) since the region served by it is higher than that for the neighbour slots. At wand 1, the behaviour was clearly asymmetrical, with higher volumetric flow rates through the slots facing the exit of filter ($\theta > 0°$; maximum equal to 0.0122 l s^{-1} at $\theta = 16.4°$) in comparison with those at $\theta < 0°$. This was a consequence of the major available area of sand on that zone. For the very same reason, higher values of volumetric flow rates were found through the slots at $\theta < 0°$ (maximum equal to 0.0111 l s^{-1} at $\theta = -16.4°$) in comparison with those at $\theta > 0°$ for wand 5. Differences between the minimum and the maximum values of flow rates through slots in a single wand were more than 100% for all underdrain positions.
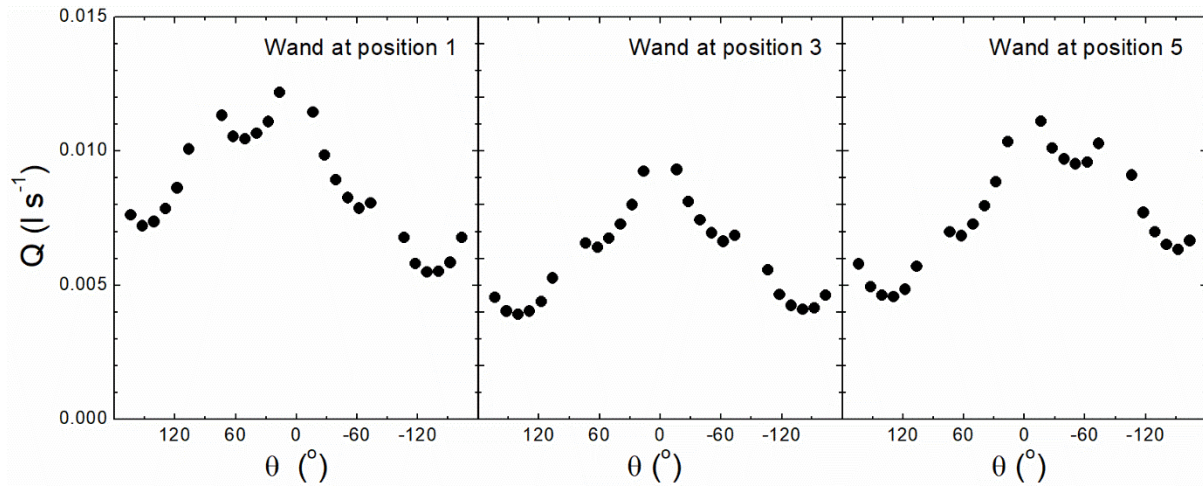
361

362 Fig. 12 - Volumetric flow rate Q in each one of the 24 slots of a single wand located at positions 1, 3

363 and 5. See Fig. 10 for the location of the wands and Fig. 3b for the angular distribution of the slots.

364

365 The total amount of volumetric flow rate per wand, weighted by the total flow rate, is shown

366 in Fig. 13 for all the experimental configurations. For example, data for case $Q = 6$ m^3 h^{-1} and

367 $H = 300$ mm were found by summing the individual contribution of each slot per wand shown

368 in Fig. 12, multiplied by 2 (since there are two wands at each position, see Fig. 10) and divided

369 by Q. The results, in percentage, clearly pointed out the hydraulics imbalance of the underdrain

370 system. Wands at position 1 were responsible of ~ 25% of water circulation, whereas those at

371 the central position ($x = 0$ m) only contributed ~ 17%. The existence of a predominant filtration

372 zone within the media enhanced the probability of partial clogging and slot damaging, and

373 increased the head loss of the entire system. Note that this preferential circulation for the first

374 wand was more remarkable when the flow rate increased. This suggests that the exit collector

375 has a significant influence on the observed imbalance.

376

377

17
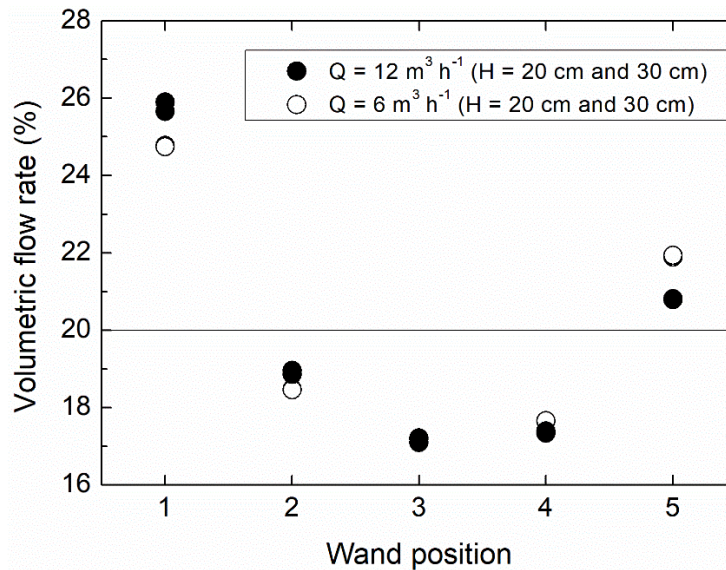
378

379   Fig. 13 - Volumetric flow rate through the wands with respect to the total one (in %) for all cases

380   simulated. Two wands are taken into account at each position (as in Fig. 10). A value of 20% is

381   expected in a filter with perfectly equilibrated wands.

382

383

384   3.2 New filter designs

385   Ideal hydraulic behaviour should balance the volumetric flow rate through each underdrain,

386   giving a value of 20% in Fig. 13 for all wand locations. The purpose here is to propose new

387   designs, that are easy to implement, to improve hydraulic behaviour in the underdrain. From

388   the previous discussion of the results, the designs investigated are based on the following two

389   hypotheses: 1) an equal horizontal area of media served per unit of underdrain would tend to

390   balance the flow rate among wands; 2) an increase in the slot open area in those underdrains

391   with less flow rates would also tend to balance the flow rate among wands. Therefore, two

392   modifications of the original filter were investigated: 1) wands spatially distributed in order to

393   cover the same horizontal area (equal area design); 2) longer wands at locations 2, 3 and 4

394   (longer wands design).

395   The wand arrangement of the equal area design is detailed in Fig. 14B. For simplicity, we

396   assumed that the horizontal area served per wand can be delimited by lines parallel to its

397   centreline. Each one of these areas was equal to 19,600 mm^2 (= $\pi D^2/40$ with $D = 0.5$ m the

398   filter inner diameter). Each wand was positioned such that its centreline points towards the

399   centroid of the served area. The calculation of distances for this case is based on a sand only

400   horizontal surface (i.e., ignoring the area covered by the exit pipe and the wands themselves).

18

401   This is the most reasonable scenario since it represents the actual situation just 25 mm above

402   the wand centreline.
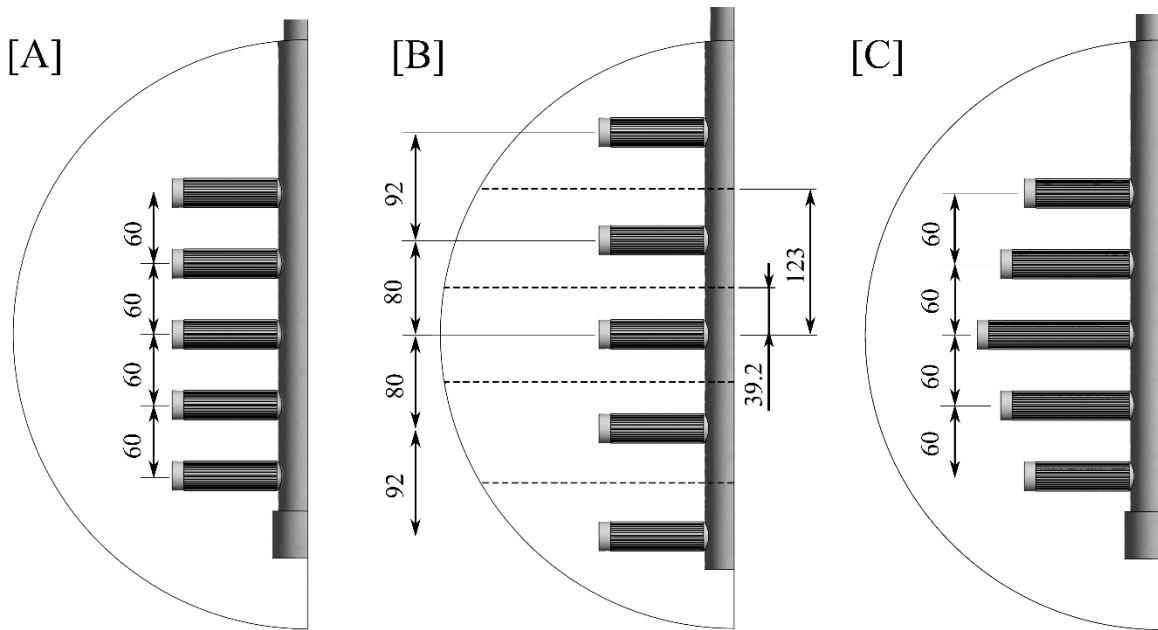
403

404   Fig. 14 - Spatial distribution of wands in the [A] original filter, [B] filter with uniform horizontal area

405   served per wand, and [C] filter with longer central wands. In [C], slots of wands at position 2, 3 and 4

406   are 20 mm, 40 mm and 20 mm longer than the original, respectively. Dimensions in mm.

407

408   The spatial distribution of the three underdrain designs here analysed is schematically shown

409   in Fig. 14. In comparison with the original case (Fig. 14A), the longer wands case (Fig. 14C)

410   enlarged the slot area by 20 mm in wands 2 and 4 and by 40 mm in wand 3. These were the

411   three wand locations with volumetric flow rates less than the expected uniform value in the

412   original filter (see Fig. 13). In contrast, the equal area design (Fig. 14B) required a slight

413   modification at the blind end of the exit collector, since it was too short to include a new

414   location for wand 5.

415   Table 2 summarises the main geometrical modifications of the underdrain designs here studied.

416   A_{wi} for $i = 1, 2, \ldots, 5$ corresponds to the horizontal area served per wand at position i, being $i =$

417   1 the closest location to the filter exit. The averaged value of the horizontal area served per

418   wand is A_{wavg}. The coefficient of variation c_v was calculated by dividing the standard deviation

419   of the A_{wi} series by A_{wavg} (Burt, 2010). $c_v = 0$ means areas equally distributed per wand. On the

420   other hand, the area covered ratio r_{ac} was calculated by dividing the horizontal area occupied

421   by the wand (projection onto the horizontal plane) by the total surface area (Burt, 2010). In this

422   case, longer wands had larger r_{ac} values although having the same coefficient of variation c_v

423   (e.g., original vs longer wands designs). Finally, the total slot open area is a characteristic of

19

424   the filter underdrain, being 20% higher for the longer wands design compared with both the
425   original and equal area cases. Note that the total slot open area was 7.3 (original and equal area
426   cases) or 8.8 (longer wands) times the cross-sectional area at filter inlet.

427

428

429   Table 2. Horizontal area served per wand A_{wi} and averaged value A_{wavg}, coefficient of variation c_v,
430   horizontal area covered ratio r_{ac} and total slot open area of the three underdrain designs analyzed.

Design	A_{w1} (mm²)	A_{w2} (mm²)	A_{w3} (mm²)	A_{w4} (mm²)	A_{w5} (mm²)	A_{wavg} (mm²)	c_v (-)	r_{ac} (-)	Open area (mm²)
Original	27,100	14,500	15,000	14,500	27,100	19,600	0.346	0.115	9,600
"Equal area"	19,600	19,600	19,600	19,600	19,600	19,600	0.000	0.115	9,600
"Longer wands"	27,100	14,500	15,000	14,500	27,100	19,600	0.346	0.135	11,520

431

432   Volumetric flow rate per wand position (expressed in % of the total flow) for the three filter
433   designs is shown in Fig. 15. For both $Q = 6$ m³ h⁻¹ and $Q = 12$ m³ h⁻¹ cases, the equal area
434   design substantially reduced the differences of flow among wands. Wand 1 maintained the
435   maximum contribution, although with a remarkable reduction (> 10%) in comparison with the
436   original filter. Numerical values are found in Table 3, where the range between the maximum
437   Q_{wmax} and the minimum Q_{wmin} flow rates per wand is < 3.3% ($Q = 6$ m³ h⁻¹) and <5.5% ($Q = $
438   12 m³ h⁻¹). By contrast, the original filter had ranges > 7.5% for all cases. The longer wands
439   case, with a 20% more slot open area than the original configuration (Table 2), also reduced
440   the contribution of the first wand almost to the same level as in the equal area design. However,
441   the high increase in the slot open area at the central wand (+50% in comparison with the
442   original one) led to a contribution to the total flow rate above 20% in all cases with wand 4
443   now being the one that contributed least to the total flowrate. As already observed in the
444   original case, almost no differences in the hydraulics behaviour of wands was observed
445   between the 200 mm and 300 mm sand height cases.

446
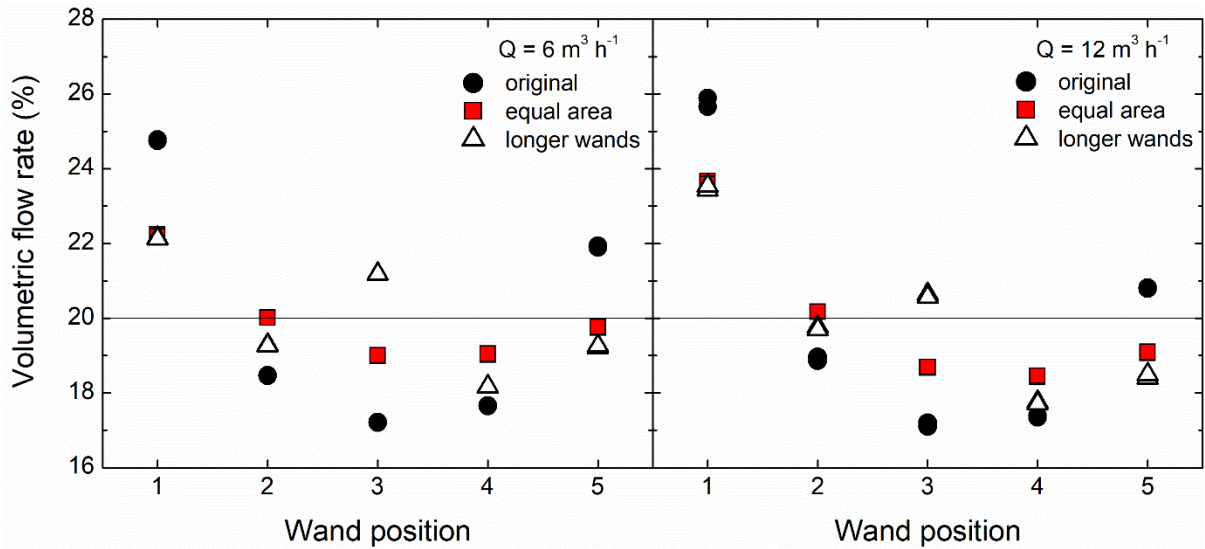
Fig. 15 - Volumetric flow rate through wands with respect to the total one (in %) for $Q = 6$ m^3 h^{-1} and 12 m^3 h^{-1} for: original filter (closed circles), filter with equal horizontal area served per wand (red squares), filter with longer wands at the centre (blue triangles) (see Fig. 15). Two wands are taken into account at each position. A value of 20% is expected in a filter with perfectly equilibrated wands.

A better balance of the flow that circulates through wands reduced the pressure drop across the filter Δp_f. The spatial redistribution of current wands in order to serve equal horizontal areas reduced the pressure drop up to 5.8% in comparison with the original design (Table 3). The longer wands design also improved the pressure drop although with more moderate values (up to 5.2%). The change in the pressure field within the sand media due to the new underdrain designs can be seen in Fig. 17 at different vertical x-z planes. The plane at $y = 65$ mm is at the centre of the slots whereas that at $y = 115$ mm is located at the end of the wand. In the equal areas design, the effect of the underdrain on the pressure contours was substantially reduced. In Fig. 16, the 202 kPa contour line of the original filter was clearly deflected from the horizontal near the filter walls. In contrast, this deflection began to be observed at the 198 kPa contour for the equal areas design. Thus, the redistribution of wands made the flow more uniform within the filter medium, diminishing the pressure drop. For the longer wands case, the zone of influence of the underdrain was similar to that from the original case. However, the pressure drop was reduced due to the increase in slot open area and, also, in the r_{ac} value.

Table 3. Maximum Q_{wmax} and minimum Q_{wmin} volumetric flow rate per wand, filter pressure drop Δp_f and its difference with respect to the original design $\Delta (\Delta p_f)$ for the three underdrain designs analyzed under different working conditions.

21

Design	$Q_{w\max}$ (%)	$Q_{w\min}$ (%)	$Q_{w\max} - Q_{w\min}$ (%)	Δp_f (Pa)	$\Delta (\Delta p_f)$ (%)
$Q = 6 \text{ m}^3 \text{ h}^{-1}$; $H = 200$ mm					
Original	24.8	17.2	7.6	15,930	
"Equal area"	22.3	19.0	3.3	15,025	-5.7
"Larger wands"	22.1	18.2	3.9	15,106	-5.2
$Q = 6 \text{ m}^3 \text{ h}^{-1}$; $H = 300$ mm					
Original	24.7	17.2	7.5	20,672	
"Equal area"	22.2	19.0	3.2	19,744	-4.3
"Larger wands"	22.1	18.2	3.9	19,859	-3.9
$Q = 12 \text{ m}^3 \text{ h}^{-1}$; $H = 200$ mm					
Original	25.7	17.2	8.5	36,712	
"Equal area"	23.7	18.4	5.3	34,567	-5.8
"Larger wands "	23.4	17.8	5.7	34,916	-4.9
$Q = 12 \text{ m}^3 \text{ h}^{-1}$; $H = 300$ mm					
Original	25.9	17.1	8.8	46,150	
"Equal area"	23.6	18.5	5.1	43,986	-4.7
"Larger wands"	23.5	17.7	5.8	44,382	-3.8

472

473

474

475
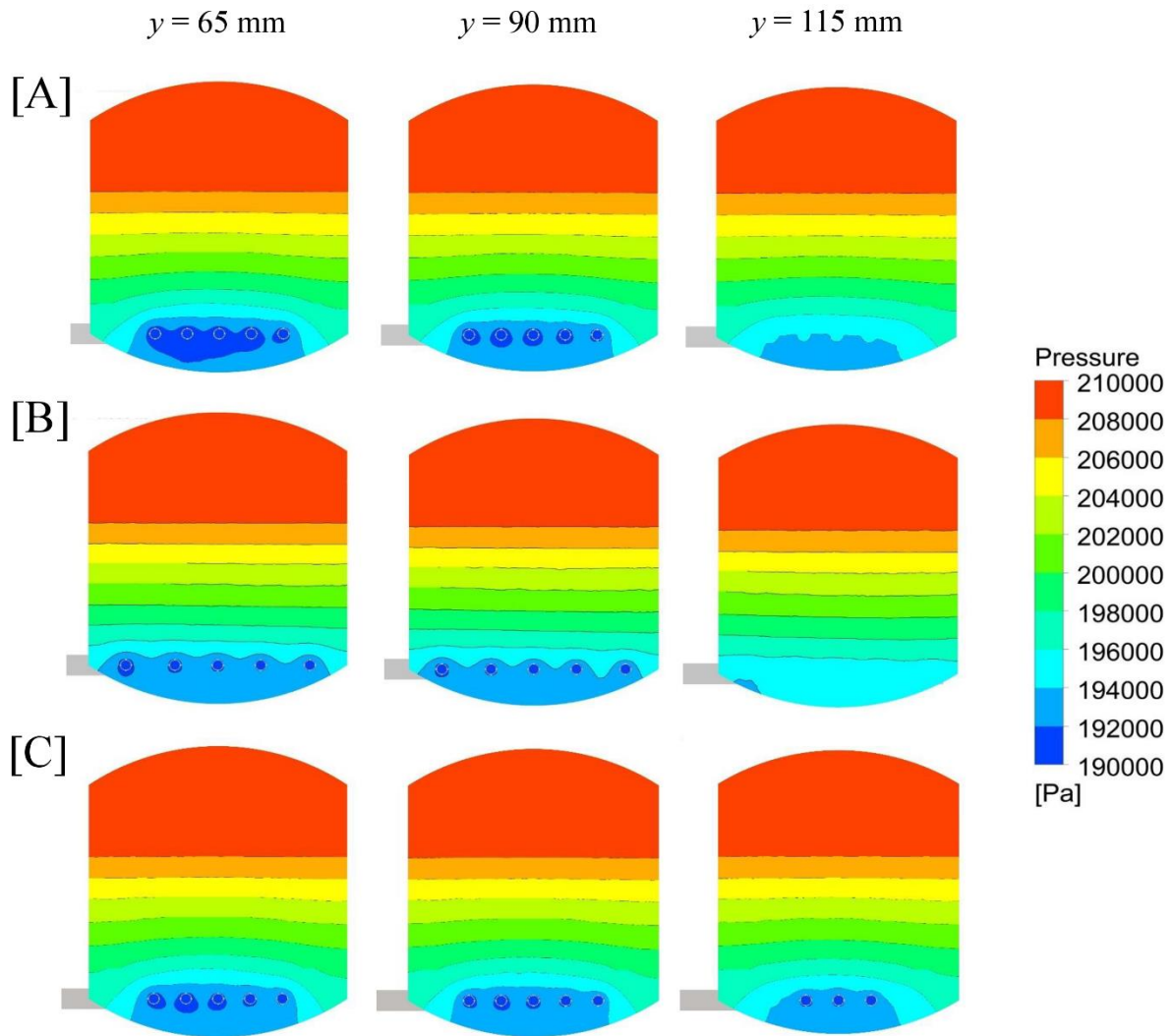
$y = 65$ mm $y = 90$ mm $y = 115$ mm

Fig. 16 - Pressure contours at different *x-z* planes ($y = 65$ mm; $y = 90$ mm and $y = 115$ mm) for different filters: [A] original filter, [B] filter with equal horizontal area served per wand, [C] filter with longer wands at the three central positions.

4. Conclusions

At the wand level, volumetric flow rates through upper slots ($-90º < \theta < 90º$) were predicted to be more than 1.4 times that through lower slots ($\theta < -90º$, $\theta > 180º$). Maximum vs minimum water flow rate ratios through slots were higher than 2.2.

At the filter level, there is also an imbalance of water flow rate among wands. Wands located closest to the pipe exit were predicted to contribute the most to the total water flow rate. The highest water velocities in the whole filter were found at the exit of these wands, where the flow joints the main stream of the collector pipe. In the original filter, wands at the centre appear to have the lowest volumetric flow rate. Differences between the maximum and the

491 minimum volumetric flow rates per wand may reach values as high as 44% (6 m^3 h^{-1} cases)

492 and 51% (12 m^3 h^{-1} cases) with respect to the lowest value (central wands).

493 A very simple and economic spatial redistribution of the original wands to serve equal

494 horizontal areas per unit underdrain is predicted to considerably improve filter performance.

495 With a coefficient of variation equal to 0, differences of volumetric flow rates among wands

496 were reduced to 17% (6 m^3 h^{-1} cases) and 28% (12 m^3 h^{-1} cases). This improvement in the

497 hydraulic equilibrium of wands implies a reduction in the filter pressure drop, being 5.7%

498 smaller than in the original filter (6 m^3 h^{-1} case).

499 Modifications of the wands in order to increase the slot open area while maintaining the original

500 spatial distribution may not be as beneficial as equalising the horizontal areas per wand. A case

501 with 20% increase in slot open area, and 18% increase in the area covered ratio per wand did

502 not improve the design with equal surface area served per wand. Therefore, the slot open area

503 value and the area covered ratio coefficient may not be as critical as the coefficient of variation

504 for determining the hydraulic performance of sand media filters with wand-type underdrains.

505

510

511 **References**

512 ANSYS, Inc. (2017). ANSYS Fluent User's Guide. Canonsburg, PA, USA: ANSYS Inc.

513 Arbat, G., Pujol, T., Puig-Bargués, J., Duran-Ros, M., Barragán, J., Montoro, L., & Ramírez

514   de Cartagena, F. (2011). Using computational fluid dynamics to predict head losses in

515   the auxiliary elements of a microirrigation sand filter. Transactions of the ASABE, 54(4),

516   1367 -1376.

517 Arbat, G., Pujol, T., Puig-Bargués, J., Duran-Ros, M., Montoro, L., Barragán, J., & Ramírez

518   de Cartagena, F. (2013). An experimental and analytical study to analyze hydraulic

519   behavior of nozzle-type underdrains in porous media filters. Agricultural Water

520   Management, 126, 64-74.

521 Bové, J., Arbat, G., Pujol, T., Duran-Ros, M., Ramírez de Cartagena, F., Velayos, J., & Puig-

522   Bargués, J. (2015). Reducing energy requirements for sand filtration in microirrigation:

523   improving the underdrain and packing. Biosystems Engineering, 140, 67–78.

524   Bové, J., Puig-Bargués, J., Arbat, G., Duran-Ros, M., Pujol, T., Pujol, J., & Ramírez de
525   Cartagena, F. (2017). Development of a new underdrain for improving the efficiency of
526   microirrigation sand media filters. Agricultural Water Management, 179, 296-305.

527   Burt, C. (2010). Hydraulics of commercial sand media filter tank used for agricultural drip
528   irrigation. ITCR Report No. R 10001. San Luis Obispo, CA, USA: Irrigation Training
529   and Research Center.

530   Célik, I.B., Ghia, U., Freitas, C.J., Coleman, H., & Raad, P.E. (2008). Procedure for estimation
531   and reporting of uncertainty due to discretization in CFD applications. Journal of Fluids
532   Engineering, 130, 078001-1–078001-4.

533   Enciso-Medina, J., Multer, W.L., & Lamm, F.R. (2011). Management, maintenance, and water
534   quality effects on the long-term performance of subsurface drip irrigation systems.
535   Applied Engineering in Agriculture, 27, 969–978.

536   Gamri, S., Soric, A., Tomas, S., Molle, B., & Roche, N. (2014). Biofilm development in
537   microirrigation emitters for wastewater use. Irrigation Science, 32 (1), 77-85.

538   Green, O., Katz, S., Tarchitzky, J., & Chen, Y. (2018). Formation and prevention of biofilm
539   and mineral precipitate clogging in drip irrigation systems applying treated wastewater.
540   Irrigation Science, 36 (4-5), 257-270.

541   ICID (2019). Annual reports for 2018-2019 and 2013-2014New Delhi, India: International
542   Commission on Irrigation and Drainage (ICID).

543   Lamm, F.R. & Rogers, D.H. (2017). Longevity and performance of a subsurface drip irrigation
544   system. Transactions of the ASABE, 60(3), 931-939.

545   Lili, Z., Yang, P., Ren, S., Li, Y., Liu, Y., & Xia, Y. (2016). Chemical clogging of emitters and
546   evaluation of their suitability for saline water drip irrigation. Irrigation and Drainage,
547   65(4), 439-450.

548   Mesquita, M., de Deus, F.P., Testezlaf, R., da Rosa, L.M., & Diotto, A.V. (2019). Design and
549   hydrodynamic performance testing of a new pressure sand filter diffuser plate using
550   numerical simulation. Biosystems Engineering, 183, 58-69.

551   Mesquita, M., Testezlaf, R., & Ramirez, J. (2012). The effect of media bed characteristics and
552   internal auxiliary elements on sand filter head loss. Agricultural Water Management,
553   115, 178-185.

554   Mesquita, M., Testezlaf, R., de Deus, F.P., & da Rosa, L.M. (2017). Characterization of flow
555   lines generated by pressurized sand filter underdrains. Chemical Engineering
556   Transactions, 58, 715-720.

557 Nakayama, F.S., Boman, B.J., & Pitts, D.J. (2007). Maintenance. In: F.R. Lamm, J.E Ayars, &
558   F.S. Nakayama, F.S. (Eds.), Microirrigation for Crop Production. Design, Operation, and
559   Management (pp. 389-430). Amsterdam, Netherlands: Elsevier.

560 Pujol, T., Arbat, G., Bové, J., Puig-Bargués, J., Duran-Ros, M., Velayos, J., & Ramírez de
561   Cartagena, F. (2016). Effects of the underdrain design on the pressure drop in sand filters.
562   Biosystems Engineering, 150, 1-9.

563 Solé-Torres, C., Puig-Bargués, J., Duran-Ros, M., Arbat, G., Pujol, J., & Ramírez de Cartagena,
564   F. (2019a). Effect of underdrain design, media height and filtration velocity on the
565   performance of microirrigation sand filters using reclaimed effluents. Biosystems
566   Engineering, 187, 292-304.

567 Solé-Torres, C., Puig-Bargués, J., Duran-Ros, M., Arbat, G., Pujol, J., & Ramírez de Cartagena,
568   F. (2019b). Effect of different sand filter underdrain designs on emitter clogging using
569   reclaimed effluents. Agricultural Water Management, 223, 105683.

570 Tarjuelo, J.M. Rodríguez-Díaz, J.A., Abadía, R., Camacho, E., Rocamora, C., & Moreno, M.A.
571   (2015). Efficient water and energy use in irrigation modernization: lessons from
572   Spanish case studies. Agricultural Water Management, 162, 67-77.

573 Trooien, T.P., & Hills, D.J. (2007). Application of biological effluent. In: F.R. Lamm, J.E.
574   Ayars, & F.S. Nakayama (Eds.), Microirrigation for Crop Production. Design, Operation,
575   and Management (pp. 329-356). Amsterdam, Netherlands: Elsevier (Chapter 9).

576

577